Mode-selective anharmonicity induced by lone-pair electrons in layered oxyselenides

Gan Liu,[1,*] Yang-Yang Lv,[2,3,*] Zhiwei Jiang,[2,3] Guan-Zhang Liu,[2,3] Xiaoli Zhou,[2,3] Yong Zhang,[2,3] Jiahui Zheng,[2,3] Lu Xu,[2,3] Ming-Hui Lu,[2,3] Shu-Hua Yao,[2,3,†] Yanbin Chen,[1,3] Jian Zhou,[2,3,‡] Xiaoxiang Xi,[1,3,§] and Yan-Feng Chen[2,3]

[1]*National Laboratory of Solid State Microstructures and Department of Physics, Nanjing University, Nanjing 210093, China*

[2]*National Laboratory of Solid State Microstructures and College of Engineering and Applied Sciences, Nanjing University, Nanjing 210093, China*

[3]*Collaborative Innovation Center of Advanced Microstructures, Nanjing University, Nanjing 210093, China*

(Received 26 June 2023; accepted 19 December 2023; published 9 January 2024)

Materials with low thermal conductivity are essential for thermoelectric energy conversion and thermal management applications. Lone-pair electrons (LPEs), a pair of nonbonded electrons, is generally believed to increase the phonon anharmonicity, which leads to low lattice thermal conductivity. However, the specific manifestation of LPEs on the lattice dynamics and phonon transport remains elusive. Here, using Raman scattering and first-principles calculations, we unveil mode-selective anharmonicity caused by LPEs in layered oxyselenides, quantified by the linewidth of Raman-active phonon modes. Strong anharmonicity is observed not only for the phonon modes associated with the ions that contain LPEs, but also for those modes involving ions that are bonded with the LPE-containing ions. The strength of anharmonicity also depends on the vibrational directions of the phonon modes. These results establish a general guideline for identifying LPE-induced anharmonicity and provide a new perspective on optimizing thermoelectric performance.

DOI: 10.1103/PhysRevB.109.024302

I. INTRODUCTION

Materials with low lattice thermal conductivity (κ_L) play an important role in many practical applications, such as thermoelectric devices and thermal barrier coatings [1,2]. To achieve low κ_L, the general guiding principle is to search for crystalline materials with complex crystal structures, heavy atomic masses, weak chemical bonds, and large phonon anharmonicity [1–3], whereas nanostructural composites [4] and superionic materials [5] also represent promising directions. Lone-pair electrons (LPEs) are an important mechanism for generating strong phonon anharmonicity because their chemically inactive nature can induce substantial local lattice distortion. Their formation requires specific cations in a certain valence state, and the cation-anion interaction governs their expression [6–8], leading to structural asymmetry about the LPE-bearing cations. Although the presence of LPEs has been commonly associated with low κ_L [6,9–14], their clear experimental fingerprint on the lattice anharmonicity remains to be uncovered, which is essential for elucidating their impact on the lattice dynamics and phonon transport [15,16].

Recently, [Bi_2O_2]-based materials, such as Bi_2O_2Ch and BiCuChO (Ch = S, Se, and Te), have received enormous attention due to their ultrahigh electron mobility [17,18], robust band gap [19], excellent optoelectronic response [20], and superior thermoelectric properties with figure of merits exceeding unity after doping [21]. These materials all have Bi-O layers with LPEs on the Bi ions and ultralow κ_L of less than 2 $Wm^{-1}K^{-1}$ at room temperatures [22–25], providing a suitable platform for investigating the relationship between the LPEs and κ_L, but existing studies are scarce. A computational study of Bi_2O_2S uncovered an eightfold enhancement in κ_L under high pressure accompanied by a structural transition, which was attributed to the pressure-induced suppression of the activity of LPEs and the strengthening of intra- and intermolecular interactions [26]. Another calculation ascribed the low κ_L in BiCuSeO and BiCuTeO to weakly bonded Cu ions, questioning the role of LPEs [27]. Clearly, the effect of LPEs on κ_L in these bismuth oxyselenides remains ambiguous, and its experimental manifestation warrants further study.

In this work, we focus on the layered oxyselenides, Bi_2O_2Se and BiCuSeO, to investigate the effect of LPEs on the anharmonicity and κ_L. For comparison, we also study LaCuSeO, which is isostructural to BiCuSeO. We discover mode-selective anharmonicity in all three materials, as schematically illustrated in Fig. 1(a). Specifically, strong anharmonicity was observed not only for those modes associated with LPE-containing ions vibrating in the layer plane, but also for those modes associated with the ions which are bonded with the LPE-containing ions and undergo out-of-plane vibration. This pattern is generic, as also confirmed in BiOCl and La_2O_2Se. It facilitates the identification of LPE-induced strong anharmonicity and suggests combining with other mechanisms to damp the remaining weakly anharmonic modes for the further reduction of κ_L.

II. EXPERIMENTAL AND COMPUTATIONAL METHODS

Bi_2O_2Se and BiCuSeO single crystals were grown by the chemical vapor transport (CVT) method using I_2 as a transport agent, as described in our previous reports [18,28,29]. First,

*These authors contributed equally to this work.
†shyao@nju.edu.cn
‡zhoujian@nju.edu.cn
§xxi@nju.edu.cn

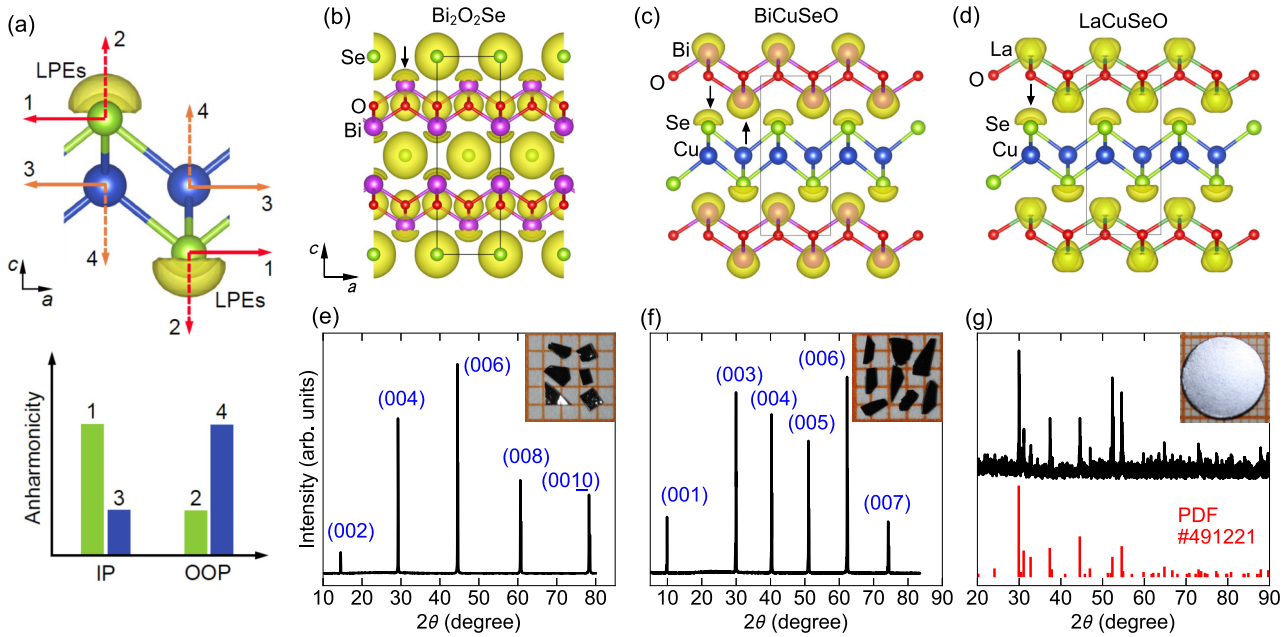

FIG. 1. (a) Schematic illustration of mode-selective anharmonicity. Modes 1 and 3 involve in-plane (IP, solid arrows) vibration of ions, whereas Modes 2 and 4 involve out-of-plane (OOP, dashed arrows) vibration of ions. LPEs: lone-pair electrons. (b)–(d) Crystal structure and calculated electron localization functions of Bi_2O_2Se (b), BiCuSeO (c), and LaCuSeO (d). The black arrows indicate the LPEs. Unit cells are marked by black rectangles. (e)–(g) XRD spectra and optical photograph of as-grown Bi_2O_2Se (e) and BiCuSeO (f) single crystals and a LaCuSeO polycrystalline sample (g).

polycrystalline Bi_2O_2Se and BiCuSeO were synthesized by the direct stoichiometric solid-state reaction

$$2Bi_2O_3 + Bi_2Se_3 \rightarrow 3Bi_2O_2Se, \quad (1)$$

$$Bi + Bi_2O_3 + 3Cu + 3Se \rightarrow 3BiCuSeO. \quad (2)$$

For Bi_2O_2Se, high pure Bi_2O_3 (Sinopharm Chemical Reagent Co., Ltd, 5N) and Bi_2Se_3 (Alfa Aesar, 5N) powders were used as raw materials, and highly pure Bi (Alfa Aesar, 5N), Bi_2O_3 (Sinopharm Chemical Reagent, 4N), Cu (Sinopharm Chemical Reagent, 4N), and Se (Alfa Aesar, 5N) powders were used to synthesize polycrystalline BiCuSeO. The raw materials were mixed, ground, and sealed in the evacuated quartz tube, and heated at about 550 °C (Bi_2O_2Se) or 700 °C (BiCuSeO) for five days to obtain the target products. Secondly, a certain amount of polycrystalline mixed by about 10 mg/mL of I_2 (Alfa Aesar, 5N) was loaded into an evacuated quartz ampoule and placed in a temperature profile of 550–650 °C (Bi_2O_2Se) or 500–600 °C (BiCuSeO) to grow the crystals. After growth for 10 days, the millimeter-sized flake Bi_2O_2Se and BiCuSeO crystals with a metallic luster were successfully obtained, respectively [see Figs. 1(e) and 1(f)]. The LaCuSeO sample used in the experiment is polycrystalline ceramic. We first synthesized LaCuSeO polycrystalline powders by the direct stoichiometric solid-state reaction of high pure La (Alfa Aesar, 3N), Cu (Alfa Aesar, 4N), Se (Alfa Aesar, 5N), and La_2O_3 (Alfa Aesar, 4N) powders at about 1000 °C for 10 days, according to

$$La + La_2O_3 + 3Cu + 3Se \rightarrow 3LaCuSeO. \quad (3)$$

Then, a certain amount of LaCuSeO powder was ground and pressed into flakes with a diameter of 10 mm and a thickness of 2 mm, and heated in an evacuated quartz ampoule again at 600 °C for 12 hours to obtain the single phase LaCuSeO polycrystalline ceramic pellets [Fig. 1(g)]. All chemical reactions were carried out in evacuated quartz ampoules at a pressure of 4×10^{-6} Torr.

X-ray diffraction of Bi_2O_2Se and BiCuSeO crystals and polycrystalline LaCuSeO were performed on an x-ray diffractometer (Ultima III Rigaku) using Cu-K_α radiation with 2θ of $5 \sim 80°$. Raman spectroscopy was performed in the backscattering geometry under 532 nm laser excitation. A 40× objective lens was used to focus the laser beam of 0.4 mW to a spot size of ~1 μm. The scattered signal was directed through notch filters and detected by a grating spectrograph equipped with a liquid-nitrogen-cooled charge-coupled device. Polarization-angle dependent measurements were performed using a couple of polarizers placed upstream and downstream of the sample in the optical path, combined with a half-wave plate mounted on a rotation stage to control the polarization direction. Temperature control between 4–300 K was achieved by a closed-cycle cryostat.

The crystal structure and lattice dynamics of Bi_2O_2Se, BiCuSeO, LaCuSeO, La_2O_2Se, and BiOCl were calculated by the density-functional theory in the generalized gradient approximation implemented in the Vienna *ab initio* simulation package code [30,31]. The projected augmented-wave method [32,33] and the nonlocal optB86b van der Waals density functionals [34–36] were used in the calculations. The plane-wave cutoff energy was 520 eV throughout the calculations. The k mesh was $9 \times 9 \times 9$ and $9 \times 9 \times 4$ for Bi_2O_2Se/La_2O_2Se and BiCuSeO/LaCuSeO/BiOCl, respectively, in the structural optimization and self-consistent calculations. The lattice constants and atomic positions were optimized with the

maximal residual forces on each atom less than 0.1 meV/Å. Based on the optimized structure, the phonon dispersions, phonon linewidths, and lattice thermal conductivities of all five materials were calculated with the assistance of Phonopy [37] and Phono3py [38] codes. The $2\sqrt{2} \times 2\sqrt{2} \times 2$ and $3 \times 3 \times 2$ supercells based on the conventional cell of Bi_2O_2Se/La_2O_2Se and BiCuSeO/LaCuSeO/BiOCl were used in calculations of the phonon dispersion and lattice thermal conductivities. The q mesh was $15 \times 15 \times 15$ and $16 \times 16 \times 8$ for Bi_2O_2Se/La_2O_2Se and BiCuSeO/LaCuSeO/BiOCl, respectively, in the calculations of lattice thermal conductivities. The cutoff distances of the third-order force constants are 4 Å in the anharmonic calculations for all five materials.

III. RESULTS AND DISCUSSION

A. Crystal structure and electron localization function

Bi_2O_2Se, BiCuSeO, and LaCuSeO all share a similar layered structure consisting of alternating stacking of $[Bi_2O_2]^{2+}$/$[La_2O_2]^{2+}$ and $[Cu_2Se_2]^{2-}$/$[Se]^{2-}$ layers [Figs. 1(b)–1(d)]. The binary layered structural motif is analogous to that of α-PbO, which is well known for its expression of LPEs [7]. The calculated electron localization function (ELF) is superimposed on the crystal structures to identify the presence of LPEs [12,39]. The ELF provides a measure of the degree of electron localization in materials. It is a dimensionless index that ranges from 0 to 1, with larger values corresponding to more localized electrons. Figures 1(b)–1(d) show the calculated ELF isosurfaces with the isosurface level of 0.60, 0.85, and 0.85 for the Bi_2O_2Se, BiCuSeO, and LaCuSeO, respectively. For Bi_2O_2Se, an asymmetric lobe is located near each Bi ion as indicated by the black arrow, evidencing Bi's LPEs. For BiCuSeO and LaCuSeO, the ELFs near the Bi ions are also more asymmetric compared with that of La ions, suggesting the presence (absence) of LPEs associated with the Bi (La) ions. Moreover, the ELFs near the Se ions in BiCuSeO and LaCuSeO show clearly asymmetric lobes, indicating LPEs on the Se ions. This implies that the $[Cu_2Se_2]^{2-}$ layers in BiCuSeO and LaCuSeO also have an important effect on the low κ_L in the two materials [27].

To investigate the effect of the LPEs on the lattice dynamics, we have synthesized all three materials. The optical micrographs of as-grown Bi_2O_2Se and BiCuSeO crystals and polycrystalline LaCuSeO are shown in the inset of Figs. 1(e)–1(g). The XRD diffraction peaks of the Bi_2O_2Se and BiCuSeO crystals can be indexed as $(00L)$, L being an integer, which suggests that the exposed surface of as-grown crystals is the *ab* plane. Figure 1(g) displays the XRD pattern of a LaCuSeO ceramic, which is in good agreement with the pair distribution function (PDF) card (# 49-1221, space group $I4/m$) and indicates the absence of any secondary phase.

B. Raman mode assignment

Figures 2(a)–2(c) show the calculated phonon band structure and partial density of states (DOS) of Bi_2O_2Se, BiCuSeO, and LaCuSeO based on the harmonic approximation, which are consistent with the ones in other works [40–42]. The phonon spectra of the three materials are all divided into two groups, that is, the low-frequency acoustic and optical phonon branches below approximately 200 cm^{-1}, and the high-frequency optical phonon branches above 200 cm^{-1}. The partial DOS shows that the high-frequency branches are predominantly from the vibrations of oxygen ions, which is attributed to the smallest mass of oxygen among all elements in these materials.

Although the Raman-active phonon modes are restricted to the Γ point, they are representative of the anharmonicity in the associated phonon branches throughout the Brillouin zone (see below). Bi_2O_2Se crystallizes in a body-centered tetragonal structure with the $I4/mmm$ space group, whereas ACuSeO (A = Bi or La) adopts the simple tetragonal structure with the $P4/nmm$ space group [42–44]. All three materials have the same point group $4/mmm$ (D_{4h}). Factor group analysis predicts the following phonon modes [42–44]:

$$\Gamma_{Bi_2O_2Se} = A_{1g} + B_{1g} + 2E_g + 3A_{2u} + 3E_u, \quad (4)$$

$$\Gamma_{ACuSeO} = 2A_{1g} + 2B_{1g} + 4E_g + 3A_{2u} + 3E_u, \quad (5)$$

among which the A_{1g}, B_{1g}, and E_g modes are Raman-active.

Utilizing polarization-angle dependent Raman measurements on multiple crystal facets and assisted by our calculation results, we managed to observe and assign the complete set of Raman-active phonon modes in all three compounds at 4 K (see details in Supplemental Material Note 1 and Fig. 1 [45]). The spectra are shown in Figs. 2(g)–2(i), with the polarization directions chosen to maximize the mode intensities. For the Bi_2O_2Se and BiCuSeO single crystals, the red and green spectra were obtained on the *ab* and side planes, respectively. The vertical dashed lines indicate the mode frequencies measured at 4 K, and the number of observed modes, four for Bi_2O_2Se and eight for BiCuSeO, is consistent with the symmetry analysis. For the polycrystalline LaCuSeO, the A_{1g}^1 and E_g^3 modes are nearly degenerate according to our calculations, making them indistinguishable in the experiment. The single peak marked by the asterisk near 166 cm^{-1} in Fig. 2(i) is assigned to these two modes, and the remaining six modes are well resolved. The measured mode frequencies are indicated as dots on the phonon band structures in Figs. 2(a)–2(c), showing an overall agreement and confirming the mode assignment. Detailed comparison of the measured and calculated mode frequencies are included in Supplemental Material Note 1 [45]. Weak peaks or humps were observed at about 130 cm^{-1} and 250 cm^{-1} in Bi_2O_2Se, 250 cm^{-1} in BiCuSeO, and 50 cm^{-1} in LaCuSeO, which may arise from defects or second-order scattering.

C. Raman phonon linewidths

To investigate the phonon anharmonicity, we performed temperature-dependent Raman measurements for each material from 4 K to 300 K. Typical spectra are shown in Figs. 2(g)–2(i). We focus on the phonon linewidth, which increases upon warming because the phonons, obeying Bose-Einstein statistics, become thermally populated, and their interaction leads to the decrease of phonon lifetime—the reciprocal of phonon linewidth. The effect is the most conspicuous for the high-frequency oxygen-dominated B_{1g} and E_g modes in Bi_2O_2Se and BiCuSeO, as highlighted by the

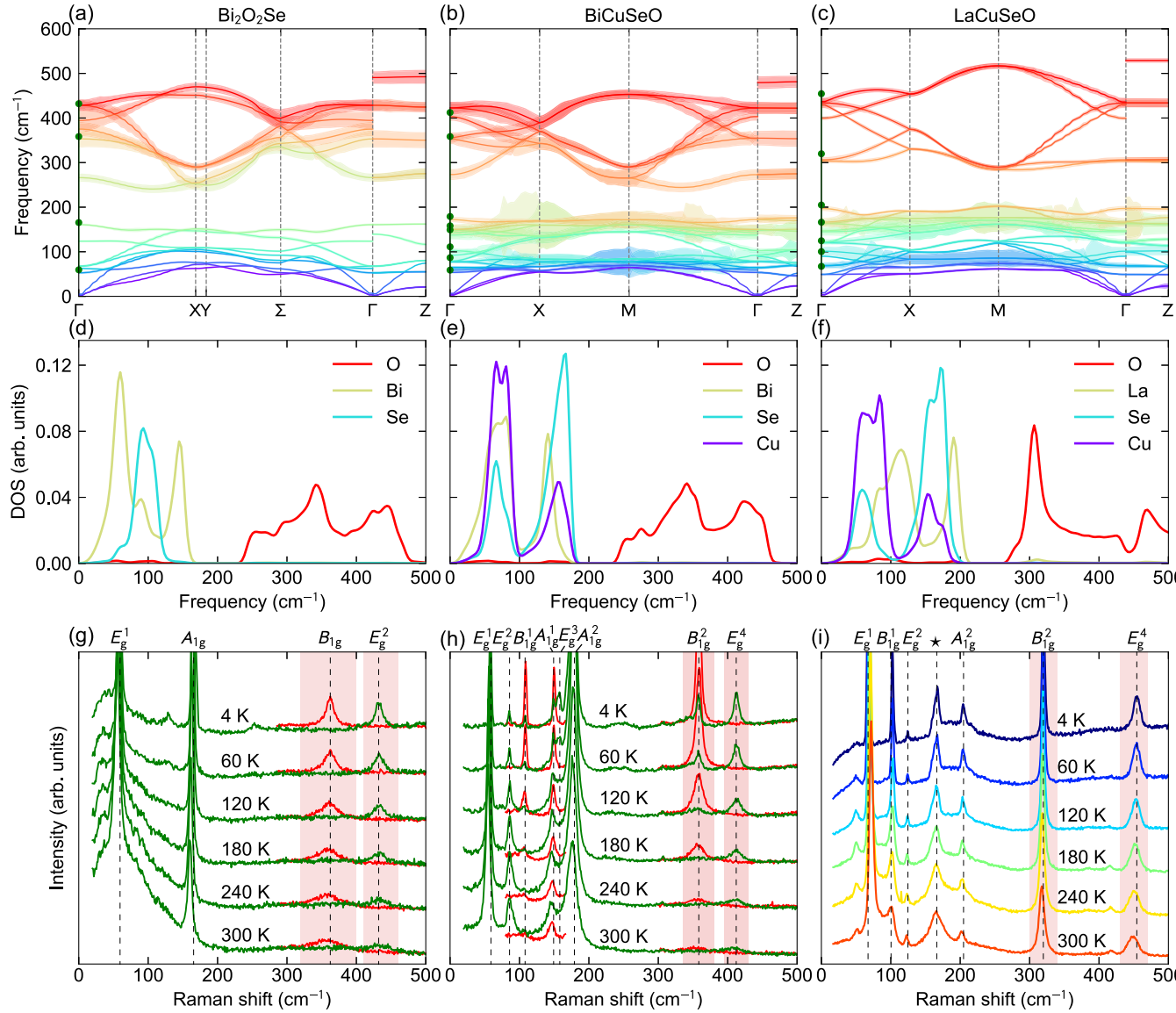

FIG. 2. (a)–(c) Calculated phonon dispersions of Bi_2O_2Se (a), BiCuSeO (b), and LaCuSeO (c). The calculated phonon linewidths at 300 K are also shown on the band structures with the transparent color ribbons. (d)–(f) The corresponding phonon partial density of states for each type of ion. (g)–(i) Temperature-dependent experimental Raman spectra. The green and red spectra in (g) and (h) were measured on the side and *ab* plane, respectively. The oxygen-dominated modes are highlighted in the shaded regions. The asterisk in (i) denotes the nearly degenerate A_{1g}^1 and E_g^3 modes. The measured Raman mode frequencies at 4 K are marked on the phonon band structures in (a)–(c) as dots. Each column corresponds to one material, as labeled on the top.

wide shaded regions in Figs. 2(g)–2(h). In contrast, the corresponding modes in LaCuSeO remain sharp within the same temperature range, suggesting that the significant broadening is related to the Bi-O layers in Bi_2O_2Se and BiCuSeO that contain LPEs. Other modes exhibiting strong broadening at high temperature include the B_{1g}^1 and E_g^3 modes in BiCuSeO. The latter is weak even at 4 K and becomes no longer observable above 100 K. Note that phonon frequency shift can also be induced by anharmonicity, but since this is further complicated by a pure-volume effect [46], we will not discuss the mode frequencies further. We have also compared two batches of Bi_2O_2Se crystals grown using different methods, which contain electron-type carrier density differing by one order of magnitude. The observed consistent Raman phonon linewidths rule out electron-phonon coupling as a major contribution to the mode broadening (Supplemental Material Note 2 and Fig. 2 [45]).

To quantify the temperature effect on the Raman spectra, we performed fitting analysis on the Raman peaks using Lorentzian functions $I(\omega) = A\gamma_j/[(\omega - \omega_j)^2 + \gamma_j^2]$, superimposed on a linear background. Here ω_j is the frequency of the jth Raman mode, $2\gamma_j$ is its linewidth (full width at half maximum), and πA is its integrated intensity. The fitted linewidths are shown in Figs. 3(a)–3(c) and the fitted frequencies are included in Supplemental Material Fig. 3 [45]. Upon warming, the phonon linewidths of all Raman modes increase due to the increased anharmonic effect. Strikingly, the linewidth of the B_{1g} (B_{1g}^2) mode in Bi_2O_2Se (BiCuSeO)

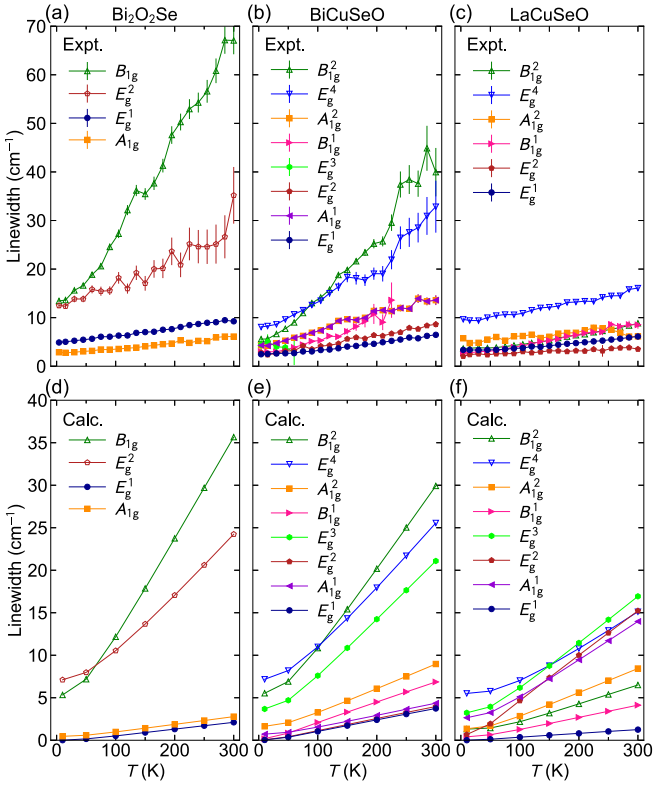

FIG. 3. (a)–(c) Temperature dependence of the experimental phonon linewidth for Bi_2O_2Se (a), BiCuSeO (b), and LaCuSeO (c). The error bars are standard deviations derived from least-squares Lorentzian fits of the phonon modes. (d)–(f) The corresponding calculated results for the three compounds. The two panels for each material share the same symbol for each mode. High-frequency oxygen-dominated modes are shown in open symbols whereas the other are shown in filled symbols.

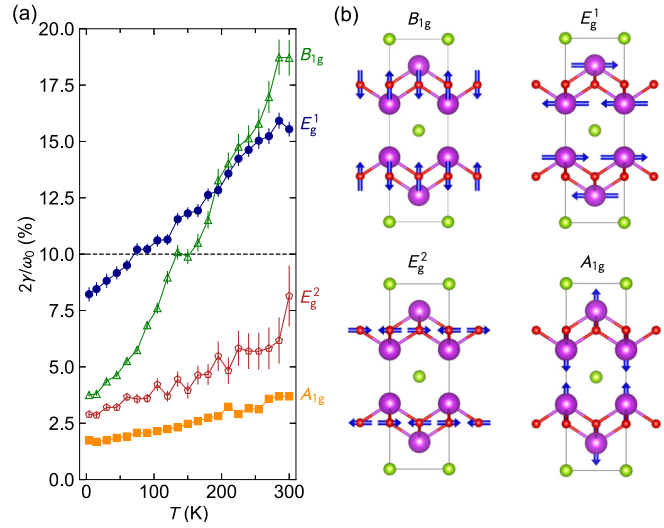

FIG. 4. (a) Temperature-dependent Raman phonon linewidths 2γ, normalized to the corresponding zero-temperature limit mode frequencies ω_0. (b) Vibration patterns for the four Raman modes of Bi_2O_2Se. The arrows represent the direction of atomic displacement.

reaches 67.1 (40.0) cm^{-1} at room temperature, which far exceeds the values in SnSe ($\sim$11 cm^{-1}) [47], the material with a record-holding thermoelectric figure of merit.

The experimentally observed linewidth broadening is nicely captured by the calculated phonon anharmonic effect according to the first-principles three-phonon method. The calculated phonon linewidths of Bi_2O_2Se, BiCuSeO, and LaCuSeO at 300 K are plotted on their phonon dispersion by the transparent color ribbon [Figs. 2(a)–2(c)]. The thickness of the color ribbon represents the phonon linewidth. The high-frequency optical phonon branches in Bi_2O_2Se and BiCuSeO exhibit large phonon linewidths, not only at the center of the Brillouin zone but also along the entire high-symmetry lines. In contrast, the corresponding phonons of LaCuSeO have significantly smaller phonon linewidths than those of BiCuSeO, although they share the same crystal structure. The acoustic and low-frequency optical phonons of BiCuSeO and LaCuSeO have much larger phonon linewidths than those of Bi_2O_2Se. This is consistent with a previous work showing that the low-frequency phonons from the copper ions have large anharmonicity and play an important role in the low thermal conductivity in BiCuSeO and BiCuTeO [27].

To compare with the experimental results, the calculated temperature-dependent Raman phonon linewidths of Bi_2O_2Se, BiCuSeO, and LaCuSeO are shown Figs. 3(d)–3(f). Although the exact calculated values differ from those obtained experimentally, the calculations well reproduce the general trend for the experimentally observed temperature dependence and even the relative magnitude of the high-frequency oxygen modes in Bi_2O_2Se and BiCuSeO. The E_g^3 mode of BiCuSeO, which is weak in the measured Raman spectra and becomes quickly overshadowed by the neighboring modes upon warming [Fig. 2(h)], is confirmed to broaden significantly in Fig. 3(e).

D. Mode-selective anharmonicity

To quantify the strength of anharmonicity and to compare its value among different modes, we propose to use a normalized phonon linewidth, namely, $2\gamma_j/\omega_{j0}$. Here, ω_{j0} is the mode frequency in the zero-temperature limit, which is unaffected by anharmonicity and is approximated by the experimental value at 4 K. This approach is justified because a high-frequency mode is bound to broaden more dramatically in general, such that its large linewidth is not necessarily related to strong anharmonicity. In an ideal three-phonon umklapp process, the phonon linewidth is given as $2\gamma_j = 2\Gamma_j^2 \frac{k_B T}{M v^2} \frac{\omega_j^2}{\omega_m}$, where Γ_j is the mode Grüneissen parameter, which effectively quantifies the anharmonicity, k_B is the Boltzmann constant, T is temperature, M is the averaged atomic mass, v is the sound velocity, and ω_m is the Debye frequency [48]. In reality, the interplay of normal and umklapp processes modifies the mode frequency dependence of the linewidth to be subquadratic [49]. Empirically, $2\gamma_j/\omega_{j0}$ provides a measure of the departure from the phonon quasiparticle picture, caused by the anharmonicity-induced renormalization of phonon self-energy [50].

We discover an interesting pattern of mode-selective anharmonicity based on the analysis of the normalized linewidth, which is best illustrated by Bi_2O_2Se. Figure 4(a) shows the

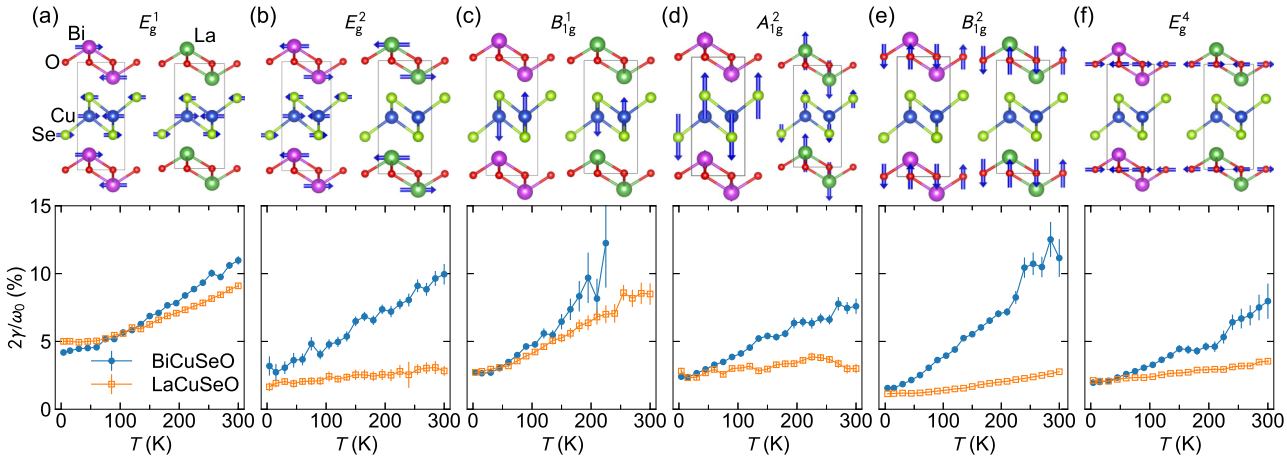

FIG. 5. (a)–(f) Temperature-dependent Raman phonon linewidths, normalized to the corresponding zero-temperature limit mode frequencies. The panels are ordered in increasing mode frequency for BiCuSeO, and the mode vibration patterns are shown on the top.

$2\gamma_j/\omega_{j0}$ for all four Raman modes in this material, which are divided into two groups at room temperature. The B_{1g} and E_g^1 modes show strong anharmonicity, with the normalized linewidth exceeding 15%. They correspond to the out-of-plane vibration of O ions and the in-plane vibration of Bi ions, respectively [Fig. 4(b)]. On the other hand, the E_g^2 and A_{1g} modes also involve these ions, but the vibrations are along the directions orthogonal to those of B_{1g} and E_g^1, respectively. Such vibrations give rise to much-reduced anharmonicity, with $2\gamma_j/\omega_{j0}$ well below 10%. Therefore, our analysis leads to the following empirical "selection rules" for strong anharmonicity [see illustration in Fig. 1(a)]: ions containing LPEs (such as Bi ions in Bi_2O_2Se) should vibrate in plane, whereas ions without LPEs (such as O ions in Bi_2O_2Se) but bonded with ions containing LPE should vibrate out of plane.

This pattern is generic, as it can also apply to BiCuSeO and LaCuSeO. Figure 5 shows $2\gamma_j/\omega_{j0}$ for six Raman modes in these materials. Overall, $2\gamma_j/\omega_{j0}$ is larger in BiCuSeO, because LPEs are more abundant in BiCuSeO [Figs. 1(c) and 1(d)]. For LaCuSeO, the La-O layers do not contain LPEs, and the related modes [Figs. 5(b), 5(d), 5(e), and 5(f)] all show weak anharmonicity, with $2\gamma_j/\omega_{j0} < 5\%$. Replacing La with Bi introduces LEPs, and the corresponding $2\gamma_j/\omega_{j0}$ for these modes at 300 K is enhanced dramatically. The behavior of mode-selective anharmonicity in BiCuSeO obeys the same rules as observed in Bi_2O_2Se, such that only the Bi and Se modes vibrating in plane [Figs. 5(a), 5(b)] and the O and Cu modes vibrating out of plane [Figs. 5(c), 5(e)] show strong anharmonicity. Likewise, the two modes in LaCuSeO associated with the LPE-containing Cu-Se layers [Figs. 5(a), 5(c)] exhibit relatively strong anharmonicity, following exactly the same rules, and the other two modes in BiCuSeO not shown in Fig. 5 are no exceptions (see Supplementary Material Fig. 4 [45]).

E. Connection with lattice thermal conductivity

Next, we establish a connection between the large normalized linewidth and low κ_L. Since the vibration frequencies of the oxygen ions are completely separated from those of other ions, we have calculated the total κ_L (Supplemental Material Table 4 [45]) and the contribution from oxygen ions (Fig. 6) at 300 K. The layered structure of all three materials indicates that the contribution of high-frequency optical phonons to the out-of-plane κ_L should be small due to their short wavelengths, such that we will just focus on the in-plane component. The in-plane total κ_L of BiCuSeO (1.69 $Wm^{-1}K^{-1}$) is much smaller than that of LaCuSeO (2.86 $Wm^{-1}K^{-1}$) due to the LPEs associated with Bi ions. The oxygen-related contribution drops remarkably from 1.32 $Wm^{-1}K^{-1}$ for LaCuSeO to 0.47 $Wm^{-1}K^{-1}$ for BiCuSeO, which is correlated with a strong enhancement of $2\gamma/\omega_0$ for the oxygen-dominated modes, particularly for the one with B_{1g} symmetry (Fig. 6). However, the contribution from other ions only slightly reduces from 1.54 $Wm^{-1}K^{-1}$ for LaCuSeO to 1.22 $Wm^{-1}K^{-1}$ for BiCuSeO, possibly mainly due to the mass increase from La to Bi ions. The connection between the large $2\gamma/\omega_0$ and low κ_L associated with the oxygen-related

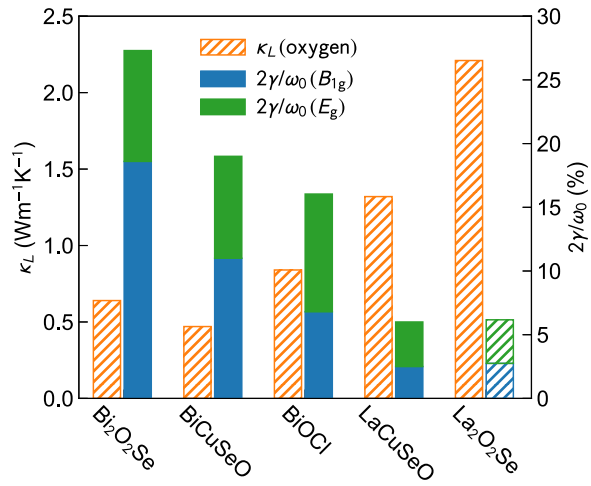

FIG. 6. Lattice thermal conductivity and normalized phonon linewidth for oxygen-related modes. The lattice thermal conductivity κ_L is the value contributed only by oxygen ions at 300 K. The normalized phonon linewidths $2\gamma/\omega_0$ are values for the high-frequency oxygen-dominated modes at 300 K. The filled and hatched bars represent measured and calculated results, respectively.

modes in Bi_2O_2Se is also shown in Fig. 6, which demonstrates the suppression of κ_L due to strong anharmonicity.

We further extend our study to include other $[Bi_2O_2]$- and $[La_2O_2]$-based layered materials [51], which confirm that our finding is universal. The oxygen-related B_{1g} and E_g Raman modes in BiOCl also show large phonon linewidths of about 27.3 and 48.5 cm^{-1} at 300 K, respectively, according to our Raman results (Supplemental Material Fig. 5 [45]), which are consistent with reported results [52]. Its in-plane oxygen-contributed κ_L is relatively small (0.84 $Wm^{-1}K^{-1}$). In comparison, La_2O_2Se has much smaller $2\gamma/\omega_0$ and much larger κ_L (2.21 $Wm^{-1}K^{-1}$) for the oxygen-related Raman modes. Note that this material is difficult to synthesize, and the calculated Raman results are used here.

F. DISCUSSION

An intuitive understanding of the mode-selective anharmonicity observed here can be traced to the spatial distribution of LPEs in the layered structural units. It has been proposed earlier that LPEs cause strong anharmonicity through nonlinear repulsive electrostatic interactions with the adjacent bonding electrons [3,6]. Take Bi_2O_2Se as an example [see Fig. 1(b) and Fig. 4(b)]. The vibrations in the form of the B_{1g} and E_g^1 modes result in a closer distance between every LPE-bearing Bi ion and one of its nearest-neighbor O ions, leading to an enhanced repulsive electrostatic force and strong anharmonicity. An opposite effect is expected for the E_g^2 and A_{1g} modes due to their atomic vibration directions that are orthogonal to those of the B_{1g} and E_g^1 modes, respectively. The orientation dependence of the anharmonicity due to LPEs was in fact noted also in $NaSbSe_2$, in which the LEPs were shown to be more polarizable along a certain direction [53]. Our work uncovers an experimental manifestation of this effect, which is expected to be universal. Furthermore, Bi_2O_2Se has been reported to show ferroelectricity under in-plane strain [54–56], which echoes the close relationship between local distortion due to LPEs, incipient ferroelectricity, and strong anharmonicity [57,58].

IV. CONCLUSION

In summary, our work demonstrates Raman spectroscopy as a facile probe of phonon anharmonicity and establishes the normalized phonon linewidth for its quantitative measure. Application of the method to the layered oxyselenides leads to the discovery of mode-selective anharmonicity, which reveals effective phonon damping only for some modes vibrating along certain directions. The ion- and vibration-direction-dependent anharmonicity is a manifestation of the asymmetrically localized LPEs that are present in these materials. These results deepen the understanding of the effect of LPEs on the anharmonicity and thermal conductivity. The mode selectivity also implies that other mechanisms are required to further reduce the thermal conductivity, by inducing phonon damping in those branches which show weak anharmonicity. Therefore, our findings could be helpful in the rational design of thermoelectric materials.

ACKNOWLEDGMENTS

This work was supported by the Foundation for Innovative Research Groups of the National Natural Science Foundation of China (Grant No. 51721001), the National Natural Science Foundation of China (Grants No. 52272002, No. 51902152, No. 11874210, No. 11974163, No. 11890702, and No. 51890861), the National Key Research and Development Program of China (Grant No. 2018YFA0307000), and the Fundamental Research Funds for the Central Universities (Grant No. 0204-14380212). The numerical calculations in this paper have been done on the computing facilities in the High-Performance Computing Center (HPCC) of Nanjing University.

[1] G. J. Snyder and E. S. Toberer, Complex thermoelectric materials, Nat. Mater. **7**, 105 (2008).
[2] T. Zhu, Y. Liu, C. Fu, J. P. Heremans, J. G. Snyder, and X. Zhao, Compromise and synergy in high-efficiency thermoelectric materials, Adv. Mater. **29**, 1605884 (2017).
[3] D. T. Morelli, V. Jovovic, and J. P. Heremans, Intrinsically minimal thermal conductivity in cubic I-V-V_2 semiconductors, Phys. Rev. Lett. **101**, 035901 (2008).
[4] M. S. Dresselhaus, G. Chen, M. Y. Tang, R. G. Yang, H. Lee, D. Z. Wang, Z. Ren, J.-P. Fleurial, and P. Gogna, New directions for low-dimensional thermoelectric materials, Adv. Mater. **19**, 1043 (2007).
[5] Q. Ren, M. K. Gupta, M. Jin, J. Ding, J. Wu, Z. Chen, S. Lin, O. Fabelo, J. A. Rodríguez-Velamazán, M. Kofu, K. Nakajima, M. Wolf, F. Zhu, J. Wang, Z. Cheng, G. Wang, X. Tong, Y. Pei, O. Delaire, and J. Ma, Extreme phonon anharmonicity underpins superionic diffusion and ultralow thermal conductivity in argyrodite Ag_8SnSe_6, Nat. Mater. **22**, 999 (2023).
[6] E. J. Skoug and D. T. Morelli, Role of lone-pair electrons in producing minimum thermal conductivity in nitrogen-group chalcogenide compounds, Phys. Rev. Lett. **107**, 235901 (2011).
[7] A. Walsh and G. W. Watson, The origin of the stereochemically active Pb(II) lone pair: DFT calculations on PbO and PbS, J. Solid State Chem. **178**, 1422 (2005).
[8] W. Wan, Y. Ge, and Y. Liu, Strong phonon anharmonicity and low thermal conductivity of monolayer tin oxides driven by lone-pair electrons, Appl. Phys. Lett. **114**, 031901 (2019).
[9] C. Chang and L.-D. Zhao, Anharmoncity and low thermal conductivity in thermoelectrics, Mater. Today Phys. **4**, 50 (2018).
[10] M. K. Jana, K. Pal, U. V. Waghmare, and K. Biswas, The origin of ultralow thermal conductivity in InTe: Lone-pair-induced anharmonic rattling, Angew. Chem. Int. Ed. **55**, 7792 (2016).
[11] E. Rathore, R. Juneja, S. P. Culver, N. Minafra, A. K. Singh, W. G. Zeier, and K. Biswas, Origin of ultralow thermal conductivity in n-type cubic bulk $AgBiS_2$: Soft Ag vibrations and local structural distortion induced by the Bi $6s^2$ lone pair, Chem. Mater. **31**, 2106 (2019).
[12] A. Lou, Q.-B. Liu, and H.-H. Fu, Enhanced thermoelectric performance by lone-pair electrons and bond anharmonicity in

the two-dimensional Ge_2Y_2 family of materials with Y = N, P, As, or Sb, Phys. Rev. B **105**, 075431 (2022).

[13] M. Dutta, M. V. D. Prasad, J. Pandey, A. Soni, U. V. Waghmare, and K. Biswas, Local symmetry breaking suppresses thermal conductivity in crystalline solids, Angew. Chem. Int. Ed. **61**, e202200071 (2022).

[14] J. Zhang, D. Ishikawa, M. M. Koza, E. Nishibori, L. Song, A. Q. R. Baron, and B. B. Iversen, Dynamic lone pair expression as chemical bonding origin of giant phonon anharmonicity in thermoelectric InTe, Angew. Chem. Int. Ed. **62**, e202218458 (2023).

[15] H. Wang, G. Qin, Z. Qin, G. Li, Q. Wang, and M. Hu, Lone-pair electrons do not necessarily lead to low lattice thermal conductivity: An exception of two-dimensional penta-CN_2, J. Phys. Chem. Lett. **9**, 2474 (2018).

[16] S. Mukhopadhyay, D. J. Singh, and T. L. Reinecke, Ultralow thermal conductivity in Cs-Sb-Se compounds: Lattice instability versus lone-pair electrons, Chem. Mater. **32**, 8906 (2020).

[17] J. Wu, H. Yuan, M. Meng, C. Chen, Y. Sun, Z. Chen, W. Dang, C. Tan, Y. Liu, J. Yin, Y. Zhou, S. Huang, H. Q. Xu, Y. Cui, H. Y. Hwang, Z. Liu, Y. Chen, B. Yan, and H. Peng, High electron mobility and quantum oscillations in non-encapsulated ultrathin semiconducting Bi_2O_2Se, Nat. Nanotechnol. **12**, 530 (2017).

[18] Y.-Y. Lv, L. Xu, S.-T. Dong, Y.-C. Luo, Y.-Y. Zhang, Y. B. Chen, S.-H. Yao, J. Zhou, Y. Cui, S.-T. Zhang, M.-H. Lu, and Y.-F. Chen, Electron-electron scattering dominated electrical and magnetotransport properties in the quasi-two-dimensional Fermi liquid single-crystal Bi_2O_2Se, Phys. Rev. B **99**, 195143 (2019).

[19] C. Chen, M. Wang, J. Wu, H. Fu, H. Yang, Z. Tian, T. Tu, H. Peng, Y. Sun, X. Xu, J. Jiang, N. B. M. Schröter, Y. Li, D. Pei, S. Liu, S. A. Ekahana, H. Yuan, J. Xue, G. Li, J. Jia *et al.*, Electronic structures and unusually robust bandgap in an ultrahigh-mobility layered oxide semiconductor, Bi_2O_2Se, Sci. Adv. **4**, eaat8355 (2018).

[20] J. Wu, Y. Liu, Z. Tan, C. Tan, J. Yin, T. Li, T. Tu, and H. Peng, Chemical patterning of high-mobility semiconducting 2D Bi_2O_2Se crystals for integrated optoelectronic devices, Adv. Mater. **29**, 1704060 (2017).

[21] J. Sui, J. Li, J. He, Y.-L. Pei, D. Berardan, H. Wu, N. Dragoe, W. Cai, and L.-D. Zhao, Texturation boosts the thermoelectric performance of BiCuSeO oxyselenides, Energy Environ. Sci. **6**, 2916 (2013).

[22] R. Guo, P. Jiang, T. Tu, S. Lee, B. Sun, H. Peng, and R. Yang, Electrostatic interaction determines thermal conductivity anisotropy of Bi_2O_2 Se, Cell Rep. Phys. Sci. **2**, 100624 (2021).

[23] Q. D. Gibson, T. Zhao, L. M. Daniels, H. C. Walker, R. Daou, S. Hebert, M. Zanella, M. S. Dyer, J. B. Claridge, B. Slater, M. W. Gaultois, F. Cora, J. Alaria, and M. J. Rosseinsky, Low thermal conductivity in a modular inorganic material with bonding anisotropy and mismatch, Science **373**, 1017 (2021).

[24] Y.-L. Pei, J. He, J.-F. Li, F. Li, Q. Liu, W. Pan, C. Barreteau, D. Berardan, N. Dragoe, and L.-D. Zhao, High thermoelectric performance of oxyselenides: Intrinsically low thermal conductivity of Ca-doped BiCuSeO, NPG Asia Mater. **5**, e47 (2013).

[25] F. Li, J.-F. Li, L.-D. Zhao, K. Xiang, Y. Liu, B.-P. Zhang, Y.-H. Lin, C.-W. Nan, and H.-M. Zhu, Polycrystalline BiCuSeO oxide as a potential thermoelectric material, Energy Environ. Sci. **5**, 7188 (2012).

[26] N. Yedukondalu, T. Pandey, and S. C. Rakesh Roshan, Effect of hydrostatic pressure on lone pair activity and phonon transport in Bi_2O_2S, ACS Appl. Energy Mater. **6**, 2401 (2023).

[27] P. Vaqueiro, R. A. R. Al Orabi, S. D. N. Luu, G. Guélou, A. V. Powell, R. I. Smith, J. P. Song, D. Wee, and M. Fornari, The role of copper in the thermal conductivity of thermoelectric oxychalcogenides: do lone pairs matter?, Phys. Chem. Chem. Phys. **17**, 31735 (2015).

[28] S.-S. Chen, Y.-C. Luo, Y.-Y. Zhang, S.-T. Dong, Y.-Y. Lv, Y.-S. Cui, S.-H. Yao, J. Zhou, and Y. B. Chen, Comparisons of electrical/magneto-transport properties of degenerate semiconductors BiCuXO (X=S, Se and Te) and their electron-phonon-interaction evolution, J. Appl. Phys. **126**, 055108 (2019).

[29] L. Xu, Y.-C. Luo, Y.-Y. Lv, Y.-Y. Zhang, S. Han, S.-H. Yao, J. Zhou, Y. B. Chen, and Y.-F. Chen, An electronic phase diagram of hole-doped BiCuSeO crystals determined by transport characterization under various growth conditions, CrystEngComm **23**, 273 (2021).

[30] G. Kresse and J. Furthmüller, Efficient iterative schemes for ab initio total-energy calculations using a plane-wave basis set, Phys. Rev. B **54**, 11169 (1996).

[31] G. Kresse and J. Furthmüller, Efficiency of ab-initio total energy calculations for metals and semiconductors using a plane-wave basis set, Comput. Mater. Sci. **6**, 15 (1996).

[32] P. E. Blöchl, Projector augmented-wave method, Phys. Rev. B **50**, 17953 (1994).

[33] G. Kresse and D. Joubert, From ultrasoft pseudopotentials to the projector augmented-wave method, Phys. Rev. B **59**, 1758 (1999).

[34] M. Dion, H. Rydberg, E. Schröder, D. C. Langreth, and B. I. Lundqvist, Van der Waals density functional for general geometries, Phys. Rev. Lett. **92**, 246401 (2004).

[35] G. Román-Pérez and J. M. Soler, Efficient implementation of a van der Waals density functional: Application to double-wall carbon nanotubes, Phys. Rev. Lett. **103**, 096102 (2009).

[36] J. Klimeš, D. R. Bowler, and A. Michaelides, Van der Waals density functionals applied to solids, Phys. Rev. B **83**, 195131 (2011).

[37] A. Togo and I. Tanaka, First principles phonon calculations in materials science, Scr. Mater. **108**, 1 (2015).

[38] A. Togo, L. Chaput, and I. Tanaka, Distributions of phonon lifetimes in Brillouin zones, Phys. Rev. B **91**, 094306 (2015).

[39] J.-Y. Raty, C. Gatti, C.-F. Schön, and M. Wuttig, How to identify lone pairs, van der Waals gaps, and metavalent bonding using charge and pair density methods: From elemental chalcogens to lead chalcogenides and phase-change materials, Phys. Status Solidi RRL **15**, 2000534 (2021).

[40] C. Wang, G. Ding, X. Wu, S. Wei, and G. Gao, Electron and phonon transport properties of layered Bi_2O_2 Se and Bi_2O_2 Te from first-principles calculations, New J. Phys. **20**, 123014 (2018).

[41] S. K. Saha and G. Dutta, Elastic and thermal properties of the layered thermoelectrics BiOCuSe and LaOCuSe, Phys. Rev. B **94**, 125209 (2016).

[42] S. K. Saha, Exploring the origin of ultralow thermal conductivity in layered BiOCuSe, Phys. Rev. B **92**, 041202(R) (2015).

[43] T. Cheng, C. Tan, S. Zhang, T. Tu, H. Peng, and Z. Liu, Raman spectra and strain effects in bismuth oxychalcogenides, J. Phys. Chem. C **122**, 19970 (2018).

[44] R. Viennois, P. Hermet, M. Beaudhuin, J.-L. Bantignies, D. Maurin, S. Pailhès, M. T. Fernandez-Diaz, M. M. Koza, C. Barreteau, N. Dragoe, and D. Bérardan, Lattice dynamics study of thermoelectric oxychalcogenide BiCuChO (Ch = Se, S), J. Phys. Chem. C **123**, 16046 (2019).

[45] See Supplemental Material at http://link.aps.org/supplemental/10.1103/PhysRevB.109.024302 for polarization-angle-dependent Raman data; comparison of measured and calculated Raman mode frequencies; extra data to exclude electron-phonon coupling as the major contribution to the phonon linewidths; temperature dependence of the Raman phonon frequencies; calculated lattice thermal conductivity; normalized phonon linewidth for the E_g^3 and A_{1g}^1 modes in BiCuSeO; and Raman spectra for BiOCl showing the oxygen-related modes. The Supplemental Material also contains Refs. [59–62].

[46] P. S. Peercy and B. Morosin, Pressure and temperature dependences of the Raman-active phonons in SnO_2, Phys. Rev. B **7**, 2779 (1973).

[47] X. Gong, H. Wu, D. Yang, B. Zhang, K. Peng, H. Zou, L. Guo, X. Lu, Y. Chai, G. Wang, and X. Zhou, Temperature dependence of Raman scattering in single crystal SnSe, Vib. Spectrosc. **107**, 103034 (2020).

[48] P. G. Klemens and D. F. Pedraza, Thermal conductivity of graphite in the basal plane, Carbon **32**, 735 (1994).

[49] K. Sääskilahti, J. Oksanen, S. Volz, and J. Tulkki, Frequency-dependent phonon mean free path in carbon nanotubes from nonequilibrium molecular dynamics, Phys. Rev. B **91**, 115426 (2015).

[50] L. Xie, J. H. Feng, R. Li, and J. Q. He, First-principles study of anharmonic lattice dynamics in low thermal conductivity $AgCrSe_2$: Evidence for a large resonant four-phonon scattering, Phys. Rev. Lett. **125**, 245901 (2020).

[51] Y. Liang, X. Zhou, W. Li, and H. Peng, Preparation of two-dimensional $[Bi_2O_2]$-based layered materials: Progress and prospects, APL Mater. **9**, 060905 (2021).

[52] J. Lu, W. Zhou, X. Zhang, and G. Xiang, Electronic structures and lattice dynamics of layered BiOCl single crystals, J. Phys. Chem. Lett. **11**, 1038 (2020).

[53] M. D. Nielsen, V. Ozolins, and J. P. Heremans, Lone pair electrons minimize lattice thermal conductivity, Energy Environ. Sci. **6**, 570 (2013).

[54] M. Wu and X. C. Zeng, Bismuth oxychalcogenides: A new class of ferroelectric/ferroelastic materials with ultra high mobility, Nano Lett. **17**, 6309 (2017).

[55] T. Ghosh, M. Samanta, A. Vasdev, K. Dolui, J. Ghatak, T. Das, G. Sheet, and K. Biswas, Ultrathin free-standing nanosheets of Bi_2O_2Se: Room temperature ferroelectricity in self-assembled charged layered heterostructure, Nano Lett. **19**, 5703 (2019).

[56] W. Wang, Y. Meng, Y. Zhang, Z. Zhang, W. Wang, Z. Lai, P. Xie, D. Li, D. Chen, Q. Quan, D. Yin, C. Liu, Z. Yang, S. Yip, and J. C. Ho, Electrically switchable polarization in Bi_2O_2Se ferroelectric semiconductors, Adv. Mater. **35**, 2210854 (2023).

[57] J. P. Heremans, The anharmonicity blacksmith, Nat. Phys. **11**, 990 (2015).

[58] D. H. Fabini, R. Seshadri, and M. G. Kanatzidis, The underappreciated lone pair in halide perovskites underpins their unusual properties, MRS Bull. **45**, 467 (2020).

[59] A. L. J. Pereira, D. Santamaría-Pérez, J. Ruiz-Fuertes, F. J. Manjón, V. P. Cuenca-Gotor, R. Vilaplana, O. Gomis, C. Popescu, A. Muñoz, P. Rodríguez-Hernández, A. Segura, L. Gracia, A. Beltrán, P. Ruleova, C. Drasar, and J. A. Sans, Experimental and theoretical study of Bi_2O_2Se under compression, J. Phys. Chem. C **122**, 8853 (2018).

[60] U. J. Kim, S. H. Nam, J. Seo, M. Yang, Q. Fu, Z. Liu, H. Son, M. Lee, and M. G. Hahm, Visualizing line defects in non-van der Waals Bi_2O_2Se using Raman spectroscopy, ACS Nano **16**, 3637 (2022).

[61] Q. Zhang, C. Chen, N. Li, Q. Huang, Y. He, X. Liu, B. Wang, D. Zhang, D. Y. Kim, Y. Wang, B. Xu, and W. Yang, Pressure impact on the crystal structure, optical, and transport properties in layered oxychalcogenides BiCuChO (Ch = S, Se), J. Phys. Chem. C **122**, 15929 (2018).

[62] Y.-Y. Lv, Y. Zhou, L. Xu, Y. Luo, Y.-Y. Zhang, L. Cao, J. Zhou, Y. B. Chen, S.-H. Yao, S.-T. Zhang, Z. Yang, and Y.-F. Chen, Non-hydrostatic pressure-dependent structural and transport properties of BiCuSeO and BiCuSO single crystals, J. Phys.: Condens. Matter **33**, 105702 (2021).